

# High-Pressure Sintering of Rhombohedral Cr<sub>2</sub>S<sub>3</sub> Using Titanium–Zirconium–Molybdenum Tools

Dennis Groeneveld,\* Hendrik Groß, Anna-Lena Hansen, Torben Dankwort, Julian Hansen, Jürgen Wöllenstein, Wolfgang Bensch, Lorenz Kienle, and Jan König


The influence of sintering parameters on the physical properties and the chemical structure of rhombohedral Cr<sub>2</sub>S<sub>3</sub> (rh-Cr<sub>2</sub>S<sub>3</sub>) is investigated using high pressures and high temperatures. The densification of the powder is performed by applying the high-pressure field-assisted sintering technique/spark plasma sintering. Using a titanium–zirconium–molybdenum (TZM) alloy as sintering tool, it is possible to increase the magnitude of the applied pressure to several hundred MPa at temperatures as high as 1223 K. A relative density of up to 99.9% is achieved at a sintering temperature of 1223 K and a pressure of 395 MPa. The presence of phase-pure rh-Cr<sub>2</sub>S<sub>3</sub> is proven by X-ray diffraction analysis and transmission electron microscopy. The Seebeck coefficients of the self-doped samples change drastically with the sintering temperatures ranging between –650 and –350 μV K<sup>-1</sup>. The densities and the thermal conductivities of the sintered samples increase with increasing sintering temperatures. The electrical conductivity is largely increased compared with the thermal conductivity potentially due to the current-assisted high-pressure sintering.

2018. FAST is used for the sintering of high-temperature materials such as refractory metals, intermetallics, and high-temperature ceramics as well in nanotechnology.<sup>[2]</sup> In the field of thermoelectrics, this densification technique is most widely applied for achieving high densities and optimized properties due to the effect of nanostructures on the physical transport properties.<sup>[3,4]</sup> The FAST process is characterized by a very fast densification of materials by rapid heating of the samples while applying a uniaxial mechanical pressure.<sup>[2]</sup> Pulsed direct current (DC) flows through either the die or the sample, depending on the electrical conductivity. This leads to a direct or an indirect heating of the sample due to Joule heating. A good densification of thermoelectric materials is necessary to gain improved electrical transport properties, especially for poor electrical conductors such as chromium sulfides.<sup>[5–8]</sup> A large number of pores in poorly densified samples lead to an increase in the scattering of phonons as well as electrons, resulting in an almost similar reduction of both the electrical and thermal conductivities. In addition to an increase in the electrical conductivity, the sintering process can also influence the charge carrier concentration due to changes in the chemical composition,

## 1. Introduction

In the last decades, the interest in the field-assisted sintering technique (FAST), commonly known as spark plasma sintering (SPS), has grown heavily.<sup>[1]</sup> Using the keyword “spark plasma sintering” in “Web of Science<sup>SM</sup>,” two publications appeared in 1995, whereas 1063 scientific articles were published in

D. Groeneveld, Prof. J. Wöllenstein, Dr. J. König  
 Laboratory for Gas Sensors, IMTEK – Department of Microsystems Engineering  
 University of Freiburg  
 Georges-Koehler-Allee 102, Freiburg 79110, Germany  
 E-mail: dennis.groeneveld@imtek.uni-freiburg.de

 The ORCID identification number(s) for the author(s) of this article can be found under <https://doi.org/10.1002/adem.201900430>.

© 2019 The Authors. Published by WILEY-VCH Verlag GmbH & Co. KGaA, Weinheim. This is an open access article under the terms of the Creative Commons Attribution License, which permits use, distribution and reproduction in any medium, provided the original work is properly cited.

The article was changed on 5 October 2019 after original online publication.

The copyright line for this article was changed on 28 October 2020 after original online publication.

Correction added on 28 October 2020, after first online publication: Projekt Deal funding statement has been added.

DOI: 10.1002/adem.201900430

H. Groß, Dr. T. Dankwort, Prof. L. Kienle  
 Institute for Materials Science  
 Kiel University  
 Kaiserstr. 2, Kiel 24143, Germany

J. Hansen, Prof. W. Bensch  
 Institute of Inorganic Chemistry  
 Kiel University  
 Max-Eyth-Str. 2, Kiel 24118, Germany

Dr. A.-L. Hansen  
 Institute for Applied Materials – Energy Storage Systems – IAM-ESS  
 Karlsruhe Institute of Technology—KIT  
 Hermann-von-Helmholtz-Platz 1, Eggenstein-Leopoldshafen 76344, Germany

Prof. J. Wöllenstein, Dr. J. König  
 Fraunhofer Institute for Physical Measurement Techniques IPM  
 Heidenhofstr. 8, Freiburg 79110, Germany

the defect density, and the carrier mobility, e.g., by the crystallinity.<sup>[9,10]</sup> Therefore, it is of major interest to investigate the influence of the sintering process on the structural as well as the electronic transport properties.

Binary chromium sulfides present a class of materials with an enormous variety in composition and structure. These properties provide a promising base for structural manipulations, which can have a large influence on the electronic transport properties.<sup>[11]</sup> Generally, the structures can be derived from the NiAs-type structure (space group:  $P6_3/mmc$ ) by an ordered removal of Cr atoms from every second layer of metal atoms parallel to the crystallographic  $c$ -axis. The result is a pseudolayered structure comprised of edge-sharing  $\text{CrS}_6$  octahedra (composition:  $\text{CrS}_2$ ) and layers with Cr-vacancies in octahedral sites.<sup>[12]</sup>  $\text{Cr}_2\text{S}_3$  crystallizes in two different polymorphs, with the rhombohedral variant rh- $\text{Cr}_2\text{S}_3$  (space group:  $R\bar{3}$ ) appearing as the equilibrium phase after synthesis.<sup>[5,13]</sup> The second polymorph, trigonal  $\text{Cr}_2\text{S}_3$  (tr- $\text{Cr}_2\text{S}_3$ ; space group:  $P\bar{3}1c$ ), is usually found in samples processed via FAST.<sup>[5]</sup> The reason behind this is the rapid volatilization of sulfur and the transformation into other phases.<sup>[5,6,14]</sup> Therefore, until now only the trigonal polymorph is thermoelectrically investigated.<sup>[5,6,8,15,16]</sup> The preservation of the rhombohedral structure of  $\text{Cr}_2\text{S}_3$  can be achieved by reducing the sintering temperature while increasing the applied pressure. Normally, graphite tools in different qualities have been used for FAST, but the fracture strength limits the magnitude of the applied pressure to about 71 MPa. For the densification at several hundred MPa and high temperature, we used tools consisting of titanium–zirconium–molybdenum (TZM) alloy for the first time.

Here, we report the synthesis of rhombohedral  $\text{Cr}_2\text{S}_3$  (rh- $\text{Cr}_2\text{S}_3$ ) via a high-temperature reaction, which was milled and subsequently sintered using high-pressure FAST (HP-FAST). Although the sintering temperature was varied between 973 and 1223 K, the remaining sintering parameters were kept constant. The influence of the high thermal and mechanical stress on the crystal structure, the chemical composition, and the physical properties was investigated.

## 2. Experimental Section

### 2.1. Synthesis

The samples were prepared via high-temperature synthesis. Stoichiometric amounts of high-purity elements of chromium (Alfa Aesar, 99%) and sulfur (Alfa Aesar, 99%) were sealed in evacuated quartz ampoules ( $<10^{-4}$  mbar) and heated to 1273 K for 3 days with an intermediate annealing step at 723 K for 1 day. Afterward, the samples were cooled down to room temperature in the furnace. The opening of the ampoules and grinding of the samples in an agate mortar were done in an argon-filled glove box ( $\text{O}_2 < 1$  ppm,  $\text{H}_2\text{O} < 1$  ppm) to prevent oxidation.

### 2.2. Densification

The sintering was performed using a FAST equipment “HP D 5” from the company FCT Systeme GmbH. The main components of the used FAST apparatus (die, two punches and spacers) were made of TZM purchased from E. Wagener GmbH (cf. setup shown in **Figure 1**). The electrical conductivity of TZM was significantly higher than that of semiconductors such as rh- $\text{Cr}_2\text{S}_3$ . For this reason, the pulsed electrical DC flowed through the TZM die, which transmitted the heat produced by Joule heating to the powder.<sup>[2,17]</sup> The temperature was measured by a K-type thermocouple placed in a radial hole inside of the die, separated by a 3 mm thick graphite wall from the sample. Moreover, soft graphite foils were used to improve the temperature uniformity via a better thermal interface and prevent possible side reactions between the powder and the tools. The die and the punches were covered with graphite felt to decrease the thermal radiation. The sintering was done in argon atmosphere to avoid oxidation. An electrical pulse pattern with an on:off duty cycle of 8:4 was chosen. As mentioned previously, the current flowed through the die, consequently the effect of DC pulsing was negligible. An exemplary sintering process is shown in **Figure 1**. The displacement due to the movement of the punches along the pressure axis gave an indication of the compression during the individual

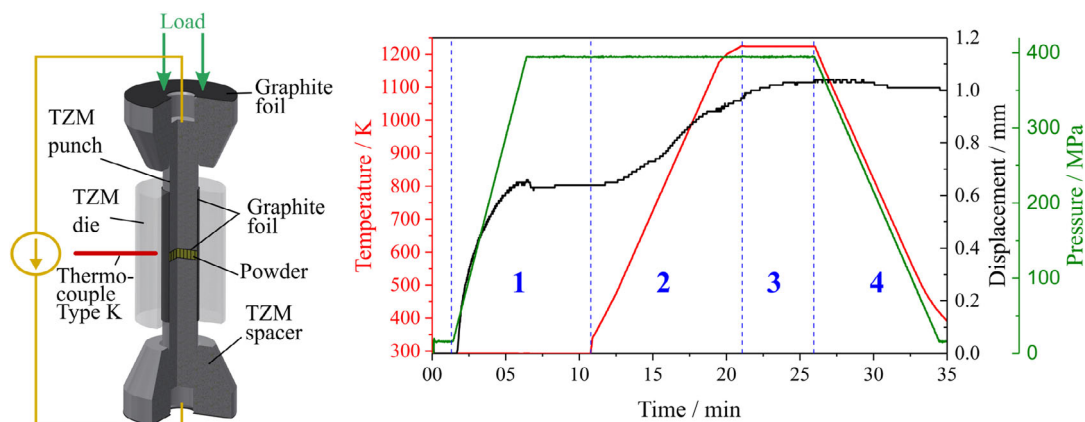


**Figure 1.** Left: A schematic model of the main components of the FAST apparatus; right: The typical sintering process shown on the sample sintered at 1223 K and 395 MPa. First, the load is applied (1), then the sample is heated (2), subsequently held at the maximum temperature (3), finally cooled down and the load is removed (4).

steps. To approximate the axial shrinkage of the sample, the sintering process was done without powder, only with graphite foil. This method determined the influence of the machine on the total displacement. Nevertheless, the thermal expansion of the powder could be neglected. In the first step (2–11 min in Figure 1), the load of 395 MPa was applied within 5 min. In the second step (11–21 min in Figure 1), the sample was heated with a heating rate of 100 K min<sup>-1</sup> to the corresponding temperature, in this case 1223 K. Before reaching the maximum temperature, the heating rate was gradually decreased to avoid overheating. The short holding time of 5 min in step 3 (21–26 min in Figure 1) was set to avoid possible evaporation of sulfur. Finally, in step 4 (26–35 min in Figure 1), the load was removed and the sample was cooled down to room temperature. Following this procedure, several samples were sintered while the temperature was varied between 973 and 1223 K in steps of 50 K.

### 2.3. Microstructural Analysis

X-ray powder diffraction (XRD) experiments were performed on a PANalytical X'Pert Pro MPD diffractometer (Cu K $\alpha_{1,2}$ , antiscatter optics (1/8° divergence slit; 1/4° antiscatter slit, secondary Ni K $\beta$  filter) in Bragg–Brentano-Geometry, using a PIXcel 1D Detector. All sintered samples were hand-ground in an agate mortar. The fundamental parameter approach was utilized to account for instrumental broadening.<sup>[18]</sup> The XRD patterns were fitted (Pawley and Rietveld refinement) using Topas Academic version 6 using model parameters given in Table 1.<sup>[19–21]</sup> Preferred (00l) orientation was taken into account using the March–Dollase model.<sup>[22]</sup> The anisotropic broadening of the Bragg reflections was modeled applying the phenomenological approach by Stephens.<sup>[23]</sup> Strain tensors were calculated using the software Wintensor 1.5 to visualize the anisotropic microstrain distribution.<sup>[24]</sup> The porosity and sulfur content were examined using scanning electron microscope (SEM) in conjunction with energy-dispersive X-ray spectroscope (EDX). These investigations were performed on a Zeiss Gemini Ultra 55 Plus, equipped with an Oxford SD EDX detector. Transmission electron microscopy (TEM) studies were performed by a FEI Tecnai F30 G<sup>2</sup> STwin equipped with a FEG operated at 300 kV. Sample preparation was performed conventionally from bulk samples, which were mechanically ground at ambient conditions and further polished in vacuum using a Gatan Precision Ion Polishing System (PIPS)

**Table 1.** Results of Rietveld refinement of Cr<sub>2</sub>S<sub>3</sub> samples sintered at given temperatures. Axial ratio for ideal hcp arrangement  $\approx 1.63$ .

Sintering temperature [K]	Lattice parameter <i>a</i> [Å]	Lattice parameter <i>c</i> [Å]	Axial ratio $\frac{c}{\sqrt{3}a}$	Volume [Å <sup>3</sup> ]
Pre SPS	5.9357(1)	16.662(6)	1.6206	508.41(2)
973	5.9374(7)	16.665(3)	1.6205	508.80(1)
1023	5.9370(7)	16.666(3)	1.6207	508.76(1)
1073	5.9370(7)	16.667(3)	1.6208	508.78(1)
1123	5.9362(6)	16.669(3)	1.6212	508.72(1)
1173	5.9362(6)	16.672(2)	1.6215	508.79(1)
1223	5.9363(6)	16.670(2)	1.6213	508.77(1)

until electron transparency was reached. Electron diffraction (ED) patterns were simulated with the software “jems version 4.5831U2017” by Stadelmann.<sup>[25]</sup> The density of the samples was determined with an Archimedes setup (ISO 5018:1983) using ethanol at room temperature. The values of the density were averaged from four measurements.

### 2.4. Thermoelectric Properties

The thermoelectric properties at room temperature were measured using equipment developed at the Fraunhofer Institute for Physical Measurement Techniques IPM. The electrical conductivity was determined applying the van der Pauw method.<sup>[26]</sup> The measurement uncertainty for the electrical conductivity was estimated to be  $\pm 0.15$  S cm<sup>-1</sup> due to the high resistance of the samples, whereas the uncertainty of the Seebeck coefficient is estimated to be  $\pm 10\%$ . The thermal conductivity was derived by

$$\lambda(T) = \rho(T) \cdot c_p(T) \cdot a(T) \quad (1)$$

with the density  $\rho$ , the specific heat  $c_p$ , and the temperature diffusivity  $a$ . The measuring of the thermal diffusivity was done with a Netzsch LFA 457 MicroFlash. The specific heat can be determined by using a reference specimen. The samples were coated with graphite to increase the emissivity and the absorbance.

## 3. Results and Discussion

### 3.1. Structural Analysis

The XRD pattern could be indexed using a rhombohedral cell in hexagonal setting, as reported by Jelinek<sup>[13]</sup> (ICSD16721, space group  $R\bar{3}$ ,  $a = 5.93$  Å,  $c = 16.67$  Å); no indications were found for the presence of the second polymorph tr-Cr<sub>2</sub>S<sub>3</sub>. A comparison of all XRD patterns after the densification and before the FAST treatment revealed an anisotropic broadening of the reflections, notably of (*hkl*)<sub>m</sub> with respect to (00l) reflections, being less pronounced in samples sintered at higher temperatures (Figure 2, right). Initial Pawley refinements revealed that this broadening could not be attributed to domain size effects. Therefore, a model by Stephens was utilized to account for *hkl*-dependent microstrain broadening.<sup>[23,27]</sup>

A 3D representation and sections through the experimentally observed tensor surfaces are shown in Figure 3. It is obvious that the distribution of the microstrain in the lattice is far from isotropic, explaining the pronounced broadening of (*hkl*) reflections. The shape of the tensor's surface is reminiscent of those observed for composition-induced microstrain as determined, e.g., for hexagonal FeN<sub>x</sub>.<sup>[27]</sup> Furthermore, the microstrain decreases with increasing sintering temperature, indicating a relaxation induced by the FAST treatment.

Details of Rietveld refinements are given in Table 1. The values of the structural parameters and the theoretical density are in good agreement with the values reported by Jelinek.<sup>[13]</sup> With increasing sintering temperature, the axial ratio shows a trend toward the ideal hcp arrangement of about 1.633. This may indicate that with increasing sintering temperature, the crystal structure is less defective.

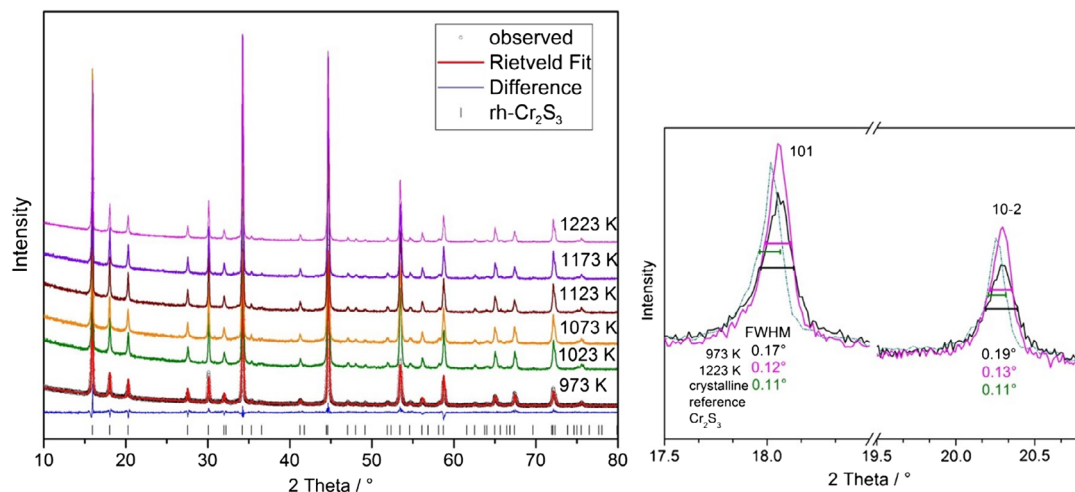


**Figure 2.** Left: Room temperature XRD pattern of  $\text{Cr}_2\text{S}_3$  sintered at different temperatures. All reflections could be indexed and refined using a rhombohedral cell (space group  $R\bar{3}$ ), represented by vertical bars. For reasons of clarity, a Rietveld fit is only shown for one pattern. Right: Enlarged region of the reflections 101 and 10-2. The reflections of the sample sintered at 973 K are clearly broader than those of the sample sintered at 1223 K. For comparison, the pattern of a crystalline reference sample is given (dashed green line).

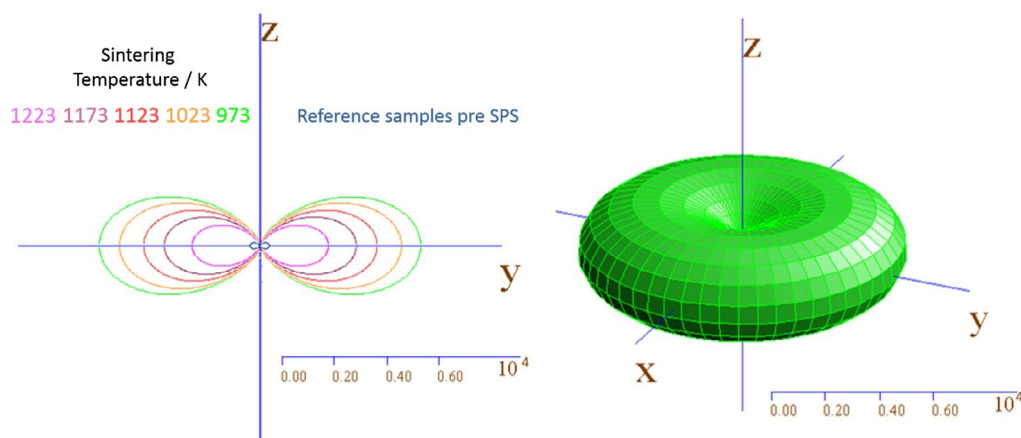


**Figure 3.** Graphical representation of experimentally determined microstrain (4th rank tensor based on hexagonal Stephens model). Left: Section through tensor surfaces projected on Cartesian coordinate X with increasing sintering temperature in comparison with a crystalline reference sample (dark blue). Right: 3D representation of tensor surface ( $\langle \Delta \epsilon_{hkl}^2 \rangle$ ) representing  $hkl$ -dependent microstrain in  $\text{Cr}_2\text{S}_3$ . Shkl parameters of the Stephens model have been used according to Leineweber.<sup>[27]</sup>  $S_{400} \rightarrow Z_{1111}$ ,  $S_{004} \rightarrow Z_{3333}$ ,  $S_{202} \rightarrow Z_{1133}$ .

Analyzing morphology, topography, and porosity of the samples using SEM images, it is evident that the use of different tools and sintering pressures as well as an increase in temperature has a tremendous effect. The SEM micrographs of the nonpolished samples show a direct comparison between samples sintered with graphite tools (Figure 4a,b) at 71 MPa and TZM tools at 395 MPa (Figure 4c–f). While the former exhibited a rough surface topography with singularly visible, loose grains and large cavities due to insufficient densification, the surface of the latter samples appeared to be significantly smoother with small, finely dispersed pores. This is especially evident when comparing samples sintered at the same temperature (Figure 4a–d, both sintered at 1073 K). Furthermore, the influence of the sintering temperature can be observed when comparing Figure 4c–f; the most regular and smoothest surface could be achieved with the highest temperature of 1223 K.

The results of EDX analyses of the samples evidence no significant deviation of the chemical composition, keeping in mind the accuracy of the method. When measured in cross-section, no stoichiometric deviation between the samples surfaces and bulk could be detected.

To investigate the influence of the sintering temperature on the micro- and nanoscopic morphology, samples treated at 973, 1023, and 1223 K were investigated by TEM. The lattice parameters and diffraction patterns of all three samples correspond well to  $\text{rh-Cr}_2\text{S}_3$ ; this phase was also confirmed for the starting material prior to sintering (cf. Figure S3, Supporting Information). In some cases, deviations from the rhombohedral symmetry occurred in ED patterns of the sintered samples, as can be seen in Figure 5. The occurring reflections with a low intensity could be attributed to the  $\text{tr-Cr}_2\text{S}_3$  structure. These deviations are independent of the sintering temperature and due to the low amount of the trigonal phase,

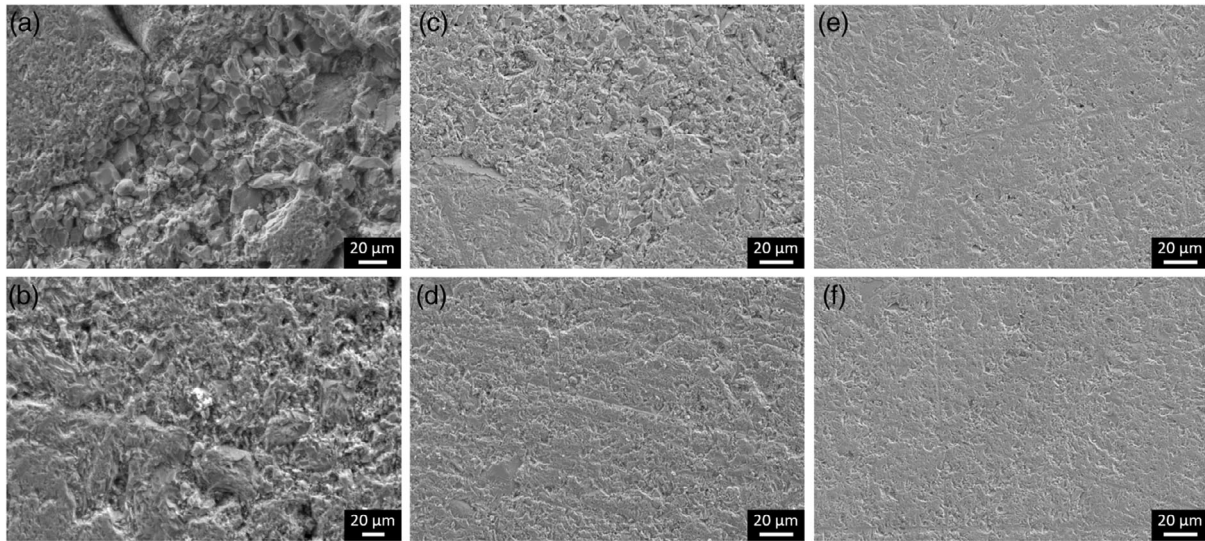


**Figure 4.** SEM surface micrographs of  $\text{Cr}_2\text{S}_3$  samples sintered at different temperatures and pressures. a,b) Sintered with graphite tools with 71 MPa at 1073 or 1173 K, respectively. For c–f), TZM tools with 395 MPa were used, whereas the sintering temperature was at (c) 973 K, (d) 1073 K, (e) 1173 K, and (f) 1223 K.

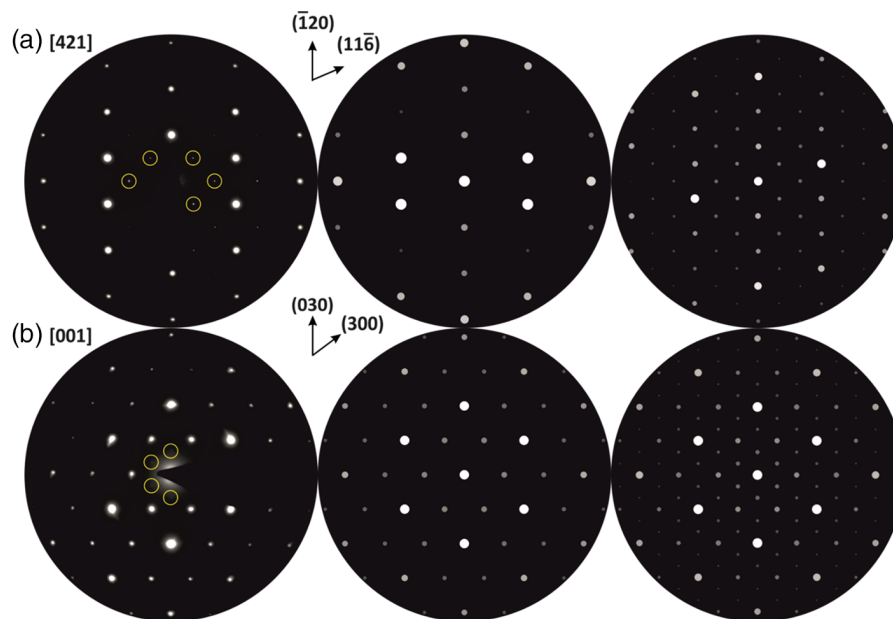


**Figure 5.** Experimental and simulated diffraction patterns of  $\text{Cr}_2\text{S}_3$  a) sintered at 973 K and 395 MPa shown in zone axis [421] and b) sintered at 1223 K and 395 MPa in zone axis [001]. The middle column represents a simulation of the corresponding zone axes of the rhombohedral  $R\bar{3}$  phase, whereas the column on the right represents the same axes simulated for the primitive  $P\bar{3}1c$  phase. Yellow circles in the experimental pattern indicate the appearance of faint additional reflections that appeared during the investigation.

no reflections could be observed using XRD. Hence, it is most likely that  $\text{tr-Cr}_2\text{S}_3$  was generated by electron-beam irradiation.

### 3.2. Density

As mentioned earlier, the sintering process with graphite tools is limited to a pressure of 71 MPa. Using this setup, the density

of  $\text{rh-Cr}_2\text{S}_3$  reached  $3.68 \text{ g cm}^{-3}$  at the highest temperature (Figure 6). However, the samples still contained pore channels, which affect the accuracy of the density measurements. By using the TZM tools, the pressure could be increased to 395 MPa. Clearly, there is a trend to higher densities at rising sintering temperatures. The density increases up to  $3.915 \text{ g cm}^{-3}$ , which corresponds to a relative density of 99.87%, considering the theoretical density of  $3.920 \text{ g cm}^{-3}$ .

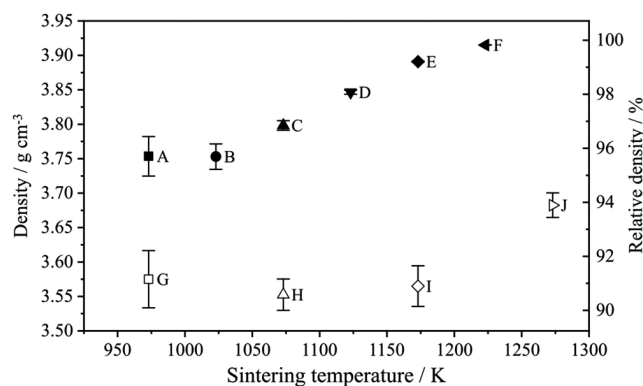


**Figure 6.** Bulk and relative density of the sintered samples. A–F were sieved <100  $\mu\text{m}$  and sintered with TZM tools. The samples G–J were not sieved and were sintered with graphite tools and a pressure of 71 MPa.

### 3.3. Electronic and Thermal Transport Properties

The electronic and thermal transport properties of the samples with low densities could not be measured due to their high porosity, whereas all samples sintered with the TZM tools could be characterized. The results are shown in Figure 7, 8, and 9 as a function of the sintering temperature. The electrical conductivity increases from 0.06 to 1.42  $\text{S cm}^{-1}$  with rising sintering temperature (Figure 7) but is still at a low level. This trend is supported by the more compact material and higher crystallinity. Due to the poor electrical properties of  $\text{Cr}_2\text{S}_3$ , it was not possible to determine the carrier concentration and mobility by Hall measurements.

The measurement results of the thermal conductivity in Figure 8 show the same trend as the electrical conductivity. With rising sintering temperature, the thermal conductivity increases due to the reasons described earlier. The ratio of the electrical to the thermal conductivity is listed in Table 2. The influence of the density on the electrical conductivity is significantly higher by a factor of  $\approx 68$  in comparison with the thermal conductivity. A reason could be the pulsed current-assisted high-pressure sintering which cause neck growth of conducting powders.<sup>[28,29]</sup>

The results of the Seebeck effect measurements at room temperature are shown in Figure 9. All samples have a large

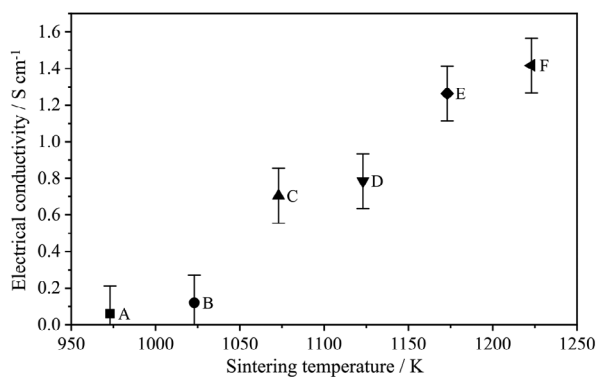


**Figure 7.** Electrical conductivity  $\sigma$  of the sintered samples as a function of the sintering temperature.

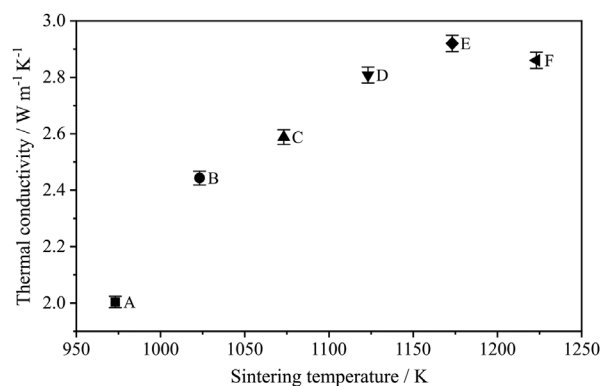


**Figure 8.** Thermal conductivity  $\kappa$  of the sintered samples as a function of the sintering temperature.

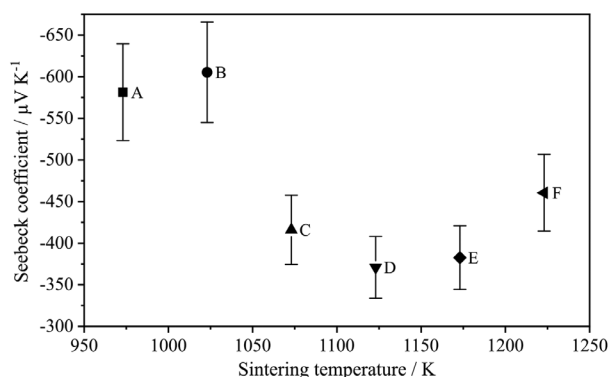


**Figure 9.** Seebeck coefficient  $\alpha$  of the sintered samples versus the sintering temperature.

thermopower, especially the samples sintered at 973 and 1023 K with a value of  $-581$  and  $-605 \mu\text{V K}^{-1}$ , respectively. The negative Seebeck coefficient indicates a n-type semiconductor where the electrons are the majority carriers. With higher sintering temperatures, the Seebeck coefficient also increases. The reason for this could not be clarified at this point.

## 4. Conclusion

By using HP-FAST, we were able to produce highly densified rh- $\text{Cr}_2\text{S}_3$  for the first time. At a sintering temperature of 1223 K and an applied pressure of 395 MPa, samples having a density of 3.915  $\text{g cm}^{-3}$  were prepared. This corresponds to a theoretical density of 99.9%. By increasing the applied pressure while simultaneously decreasing the temperature during sintering, the initial structure could be preserved. The microstrain decreases with increasing sintering temperature at constant pressures. The measurements of the electrical and thermal conductivity indicate a strong dependency of the microstructure. Higher sintering temperatures lead to less pores in the material and therefore to an enhancement of the thermal and electrical conductivities. The huge increase in the electrical conductivity compared with the thermal conductivity is referred to the formation of sintering necks during the HP-FAST process.

**Table 2.** The room-temperature properties of the rh-Cr<sub>2</sub>S<sub>3</sub> samples sintered at 395 MPa and varied temperatures.

Sintering temperature [K]	Bulk density [g cm <sup>-3</sup> ]	Relative density [%]	Electrical conductivity [S cm <sup>-1</sup> ]	Thermal conductivity [W m <sup>-1</sup> K <sup>-1</sup> ]	Seebeck coefficient [μV K <sup>-1</sup> ]	Ratio of electrical to thermal conductivity [K V <sup>-2</sup> ]
973	3.754	95.75	0.06	1.47	-581.34	4.2
1023	3.753	95.74	0.12	1.79	-605.29	6.7
1073	3.798	96.89	0.70	1.89	-416.01	37.2
1123	3.847	98.13	0.78	2.06	-370.95	38.2
1173	3.891	99.26	1.26	2.13	-382.66	59.2
1223	3.915	99.87	1.42	2.09	-460.45	67.7

Due to this effort, the thermoelectric properties of rh-Cr<sub>2</sub>S<sub>3</sub> can be optimized in the near future. Especially, the huge increase in the electrical conductivity by a factor of 68 compared with the thermal conductivity can help to improve the physical transport properties regarding thermoelectric applications. Further investigations regarding intercalation and doping to optimize the electrical conductivity as well as the formation of solid solutions will be therefore of major interests.

## Supporting Information

Supporting Information is available from the Wiley Online Library or from the author.

## Acknowledgements

The authors thank the German Research Foundation (DFG) within the research grant BE1653/36-1, KI1263/16-1, and KO5397/2-1. In addition, the authors thank A. Laptev for his helpful input to this project. Open access funding enabled and organized by Projekt DEAL.

## Conflict of Interest

The authors declare no conflict of interest.

## Keywords

chromium sulfides, field-assisted sintering technique, microstructure, spark plasma sintering, thermoelectricity

Received: April 18, 2019

Revised: July 5, 2019

Published online: September 1, 2019

[1] Z. A. Munir, U. Anselmi-Tamburini, M. Ohyanagi, *J. Mater. Sci.* **2006**, 41, 763.

- [2] O. Guillon, J. Gonzalez-Julian, B. Dargatz, T. Kessel, G. Schierning, J. Räthel, M. Herrmann, *Adv. Eng. Mater.* **2014**, 16, 830.
- [3] W.-T. Chiu, C.-L. Chen, Y.-Y. Chen, *Sci. Rep.* **2016**, 6, 23143.
- [4] B. Du, F. Gucci, H. Porwal, S. Grasso, A. Mahajan, M. J. Reece, *J. Mater. Chem. C* **2017**, 5, 1514.
- [5] A. Maignan, Y. Bréard, E. Guilmeau, F. Gascoin, *J. Appl. Phys.* **2012**, 112, 13716.
- [6] A. Maignan, E. Guilmeau, F. Gascoin, Y. Bréard, V. Hardy, *Sci. Technol. Adv. Mater.* **2012**, 13, 53003.
- [7] D. Babot, G. Peix, M. Chevreton, *J. Phys. Colloq.* **1976**, 37, C4-111.
- [8] D. Babot, M. Chevreton, *J. Solid State Chem.* **1973**, 8, 166.
- [9] J. Koenig, M. Winkler, T. Dankwort, A.-L. Hansen, H.-F. Pernau, V. Duppel, M. Jaegle, K. Bartholomé, L. Kienle, W. Bensch, *Dalton Trans.* **2015**, 44, 2835.
- [10] Z.-H. Ge, L.-D. Zhao, D. Wu, X. Liu, B.-P. Zhang, J.-F. Li, J. He, *Mater. Today* **2016**, 19, 227.
- [11] G. J. Snyder, E. S. Toberer, *Nat. Mater.* **2008**, 7, 105.
- [12] P. Vaqueiro, A. V. Powell, A. I. Coldea, C. A. Steer, I. M. Marshall, S. J. Blundell, J. Singleton, T. Ohtani, *Phys. Rev. B* **2001**, 64, 167.
- [13] F. Jellinek, *Acta Cryst.* **1957**, 10, 620.
- [14] Y.-X. Chen, B.-P. Zhang, Z.-H. Ge, P.-P. Shang, *J. Solid State Chem.* **2012**, 186, 109.
- [15] K. R. Pisharody, *J. Solid State Chem.* **1979**, 30, 149.
- [16] C. F. van Bruggen, M. B. Vellinga, C. Haas, *J. Solid State Chem.* **1970**, 2, 303.
- [17] W. Chen, U. Anselmi-Tamburini, J. E. Garay, J. R. Groza, Z. A. Munir, *Mater. Sci. Eng.: A* **2005**, 394, 132.
- [18] R. W. Cheary, A. Coelho, *J. Appl. Crystallogr.* **1992**, 25, 109.
- [19] A. Coelho, *Topas Academic*, Version 6, **2016**.
- [20] G. S. Pawley, *J. Appl. Cryst.* **1981**, 14, 357.
- [21] H. M. Rietveld, *J. Appl. Cryst.* **1969**, 2, 65.
- [22] W. A. Dollase, *J. Appl. Cryst.* **1986**, 19, 267.
- [23] P. Stephens, *J. Appl. Crystallogr.* **1999**, 32, 281.
- [24] W. Kaminsky, *Wintensor*, Version 1.5, **2014**.
- [25] P. A. Stadelmann, *Ultramicroscopy* **1987**, 21, 131.
- [26] L. J. van der Pauw, *Phillips Res. Rep.* **1958**, 13, 1.
- [27] A. Leineweber, *Z. Kristallogr.* **2011**, 226, 905.
- [28] X. Song, X. Liu, J. Zhang, *J. Am. Ceram. Soc.* **2006**, 89, 494.
- [29] K. Hu, X. Li, S. Qu, Y. Li, *Metall. Mater. Trans. A* **2013**, 44, 923.